Journal of
Materials Chemistry A

ROYAL SOCIETY
OF CHEMISTRY

PAPER

View Article Online
View Journal

Cite this: DOI: 10.1039/d5ta08096g

Rational design of aqueous zinc-ion battery electrolytes based on intermolecular interactions between co-solvents and anions

Jaehong Lim,†[ab] Hongjun Chang,†[c] In Young Jeong,[c] Minji Jeong,[a] Yiseul Yoo,[ab] Haeun Baeg,[ab] Taeeun Yim,[d] Dongjin Byun,[b] Kyung Yoon Chung,[a] Hyung-Seok Kim,[a] Janghyuk Moon*[c] and Si Hyoung Oh*[ae]

Received 3rd October 2025
Accepted 6th January 2026

DOI: 10.1039/d5ta08096g

rsc.li/materials-a

Despite their great promise as a sustainable alternative to lithium-ion batteries for stationary energy storage systems, aqueous zinc-ion batteries (AZIBs) continue to suffer from interfacial instability between metal anodes and electrolytes, stemming from the high activity of free water molecules in the electrolyte. Incorporating chaotropic co-solvents or additives with a strong affinity toward Zn has long been recognized as a viable and cost-effective approach to mitigate these issues, yet such strategies often face intrinsic miscibility limitations. To address this issue, we employed tetrahydrofuran (THF) to rationally design fully miscible electrolytes by balancing kosmotropic and chaotropic interactions between THF and anions in THF–H_2O solutions. In these systems, THF not only disrupts the hydrogen-bonding network in water clusters, but also forms robust adsorbate layers on the zinc surface, suppressing Zn metal corrosion and promoting uniform and compact Zn deposition, thereby leading to excellent long-term electrochemical performance. Furthermore, the spontaneous phase separation into THF-rich and sulfate-rich phases, driven by the salting-out effect among THF, triflate and sulfate in aqueous solution, was exploited to prepare biphasic electrolytes capable of providing tailored electrolyte environments for the cathode and anode, respectively, in Zn–I_2 batteries. This study offers new insights and opportunities to design advanced electrolytes to tackle longstanding challenges with various AZIBs.

Introduction

Driven by the rising global demand for green energy sources, safe and affordable stationary energy storage systems (ESSs) have recently attracted considerable attention to address their intermittency, a major roadblock that limits the stability of power generation and large-scale deployment of renewable energy.[1,2] To date, Li-ion batteries (LIBs) have thus far met this demand; however, they are approaching their practical limitation with respect to cost-competitiveness and safety, highlighting the urgent need for alternative solutions.[3,4]

Aqueous zinc-ion batteries (AZIBs) represent viable alternatives to LIBs, employing battery chemistries (*e.g.*, MnO_2–Zn, V_2O_5–Zn, and I_2–Zn) that provide unique benefits in terms of cost, safety and environmental sustainability.[5,6] Despite these apparent advantages, commercial adoption of AZIBs is still plagued by several key technical challenges from persistent interfacial instability between zinc metal and aqueous electrolytes.[7–9] This often leaves the metal surface unevenly passivated by the build-up of corrosion products, which in turn leads to non-uniform areal impedance growth, local hotspots for dendritic proliferation of metal deposits, and the accumulation of hydrogen gas – all of which pose serious risk to battery performance and safety.[10–12] To cope with these critical issues, numerous attempts have been made so far to protect the vulnerable surface of Zn metal such as reducing the excessive fraction of free water molecules in the electrolyte, while forming an ion-conducting protective film on the metal surface by elaborately controlling the interface *via* easily scalable electrolyte engineering.[13–15] The participation of co-solvent molecules, anions or additives into the inner coordination sphere of cations to alter the electronic structure and higher surface adsorption energies over water molecules was typically considered an important factor to secure high efficiency as well as surface uniformity. For instance, co-solvents like polyethylene

---

[a] *Energy Storage Research Center, Korea Institute of Science and Technology, Hwarang-ro 14-gil 5, Seongbuk-gu, 02792 Seoul, Republic of Korea. E-mail: sho74@kist.re.kr*

[b] *Department of Materials Science and Engineering, Korea University, 145, Anam-ro, Seongbuk-gu, Seoul 02841, Republic of Korea*

[c] *Department of Energy Systems Engineering, Chung-Ang University, Heukseok-Ro, Dongjak-Gu, Seoul 06974, Republic of Korea. E-mail: jhmoon84@cau.ac.kr*

[d] *Department of Chemistry, Incheon National University, 119 Academy-ro, Yeonsu-gu, Incheon 22012, Republic of Korea*

[e] *Division of Energy & Environment Technology, Korea University of Science and Technology, Hwarang-ro 14-gil 5, Seongbuk-gu, 02792 Seoul, Republic of Korea*

† These authors contributed equally to this work.

glycol (PEG),[16] formamide (FA),[17] dimethylacetamide (DMAC) and trimethyl phosphate (TMP),[18,19] or additives like tetra-azamacrocycle derivatives,[20] and disodium maleate molecules[21] were introduced in the aqueous electrolytes to adjust interface dynamics to obtain well-controlled (002) – textured Zn deposit and reduced corrosion rates.

Meanwhile, it is important to finely adjust the combination of salts and solvents to make the most of the beneficial effect of the co-solvent addition as it often leads to phase separation or precipitation due to nuanced changes in the intermolecular interactions among the configured electrolyte components. In the aqueous solution, the kosmotropic or chaotropic properties are considered as a primary factor that determines the miscibility of the co-solvent, where kosmotropic agents contribute to enforcing strong water–water interactions, while chaotropic ones disturb the structure.[22,23] In contrast, other studies deliberately utilized this spontaneous immiscibility among electrolyte species, as biphasic electrolytes have garnered much attention as a promising strategy to improve battery performance by providing a tailored electrolyte for each electrode.[24]

In this work, we utilized tetrahydrofuran (THF) as a co-solvent of the aqueous electrolyte to address various interfacial issues between the aqueous electrolyte and the Zn metal anode. Recently, tetrahydrofuran (THF) has been investigated as an electrolyte additive to mitigate these interfacial issues. For instance, He *et al.*[25] introduced 5 vol% THF into a 2 M $ZnSO_4$ electrolyte and You *et al.*[26] utilized a THF-water hybrid system containing $Zn(OTf)_2$ salt. These studies demonstrated that THF lowers water activity through strong hydrogen-bonding interactions, thereby optimizing the solvation structure particularly for enhancing stability at low temperatures.[26] Additionally, in a 2 M $ZnSO_4$-based electrolyte, Qiang *et al.*[27] highlighted the role of THF adsorption on the Zn anode in regulating crystal orientation and suppressing dendrite growth.

However, these studies primarily utilized THF as a functional additive without fully addressing the fundamental physicochemical interactions—specifically the chaotropic nature of THF—that dictate its miscibility with various salts. Consequently, a comprehensive framework that utilizes these molecular interactions to rationally design electrolytes, including the creation of biphasic systems for simultaneous cathode and anode protection, has yet to be established. Herein, we present a study on this strategy, offering new insights and opportunities to tackle longstanding challenges with various AZIBs.

Results and discussion

Design of electrolytes based on kosmotropic and chaotropic interactions between THF and anions

THF is a water-miscible chaotropic solvent with low viscosity (0.55 mPa s at 20 °C),[28] and high electrochemical stability towards many metal plating–stripping reactions with low electrode potentials (*e.g.*, Li, Na, and Mg) and is often employed as one constituent of common solvents or versatile additives to many rechargeable batteries.[28–30] These properties are particularly effective to mitigate the unique hydrogen bonding structure in water clusters and thus to relieve the recurring issues related with metal corrosion and hydrogen evolution in aqueous electrolytes. However, introducing ionic metal salts to co-solvents for constituting electrolyte systems often leads to prompt phase separations or eventual precipitation of insoluble adducts. These are often closely linked to the kosmotropic/chaotropic features of the co-solvents or ions in the aqueous solution.[31–33] If anions and co-solvents with significant different physicochemical properties are mixed, large repulsive intermolecular interactions ($\Delta H_{\mathrm{mix}} > 0$) can result in large positive Gibbs free energy of mixing ($\Delta G_{\mathrm{mix}} > 0$),[34] thereby causing immediate phase separation. As shown in Fig. 1a, an aqueous solution containing SO_4^{2-} anions (**ES**) which have a high charge density (high electrostatic potential, ESP), (Fig. 1b) and thus strong kosmotropic character makes a distinct phase boundary with THF solvent (termed **ES-THF-0.5**) as they decrease the solubility of nonpolar solvents. In contrast, an aqueous solution containing a chaotropic bulky OTf^- (triflate) anion (**ET**) with a low charge density was readily miscible with THF as chaotropic OTf^- (**ET-THF-0.5–3.5**) breaks down the water clustering structure and increases the solubility of THF. Such a trend can also be inferred from the results of the Hildebrand solubility parameters for THF–H_2O–$Zn(OTf)_2$ solutions in Fig. 1c. As the THF fraction increases, the total energy associated with molecular interactions gradually decreased, reflecting the much lower solubility parameter of THF (19.5 $MPa^{0.5}$) compared to pure H_2O (47.9 $MPa^{0.5}$).[35] Therefore, the bulky OTf^- anion with a low charge density is readily soluble in THF–H_2O solution, while SO_4^{2-} with a high charge density tends to form a separate phase immiscible with THF–H_2O solution. Therefore, to take full advantage of the beneficial effect of THF mixing, chaotropic anions with low charge density such as OTf^-, $TFSI^-$ and ClO_4^- are required to make a homogeneous electrolyte solution that does not trigger a phase separation or precipitation. The detailed compositions of the electrolyte considered and the miscibility are summarized in Table S1. The changes in the portfolios of the intermolecular forces (IMF) in the electrolyte solution upon the addition of increasing amount of THF was investigated by FT-IR spectroscopy (Fig. 1d, e and S1). The fraction of strong IMFs, which is associated with hydrogen bonds in water clusters[36–38] decreases as the fraction of THF increases in the electrolyte solution containing chaotropic OTf^- anions (*e.g.*, 50.3% for **ET-THF-3.5**) compared to pure aqueous solution (58.7% for **ET**), while the solution containing SO_4^{2-} (**ES**) intensifies the fraction (73.9%). This suggests that the activity of water can be substantially reduced in THF–H_2O electrolytes with OTf^- anions, which would suppress undesired parasitic side reactions on the zinc metal surface. Raman spectroscopy further corroborates the FT-IR results by showing a consistent weakening of strong hydrogen bonding and an increase in weakly hydrogen-bonded water with increasing THF fraction (Fig. S2).

The solvation structure of Zn^{2+} in **ET-THF** electrolytes was also investigated using molecular dynamics studies (Fig. 2a). As the THF fraction increased in the THF–H_2O electrolytes, the number of coordinated water molecules gradually decreased (Fig. 2b), while a fraction of THF molecules as well as OTf^-

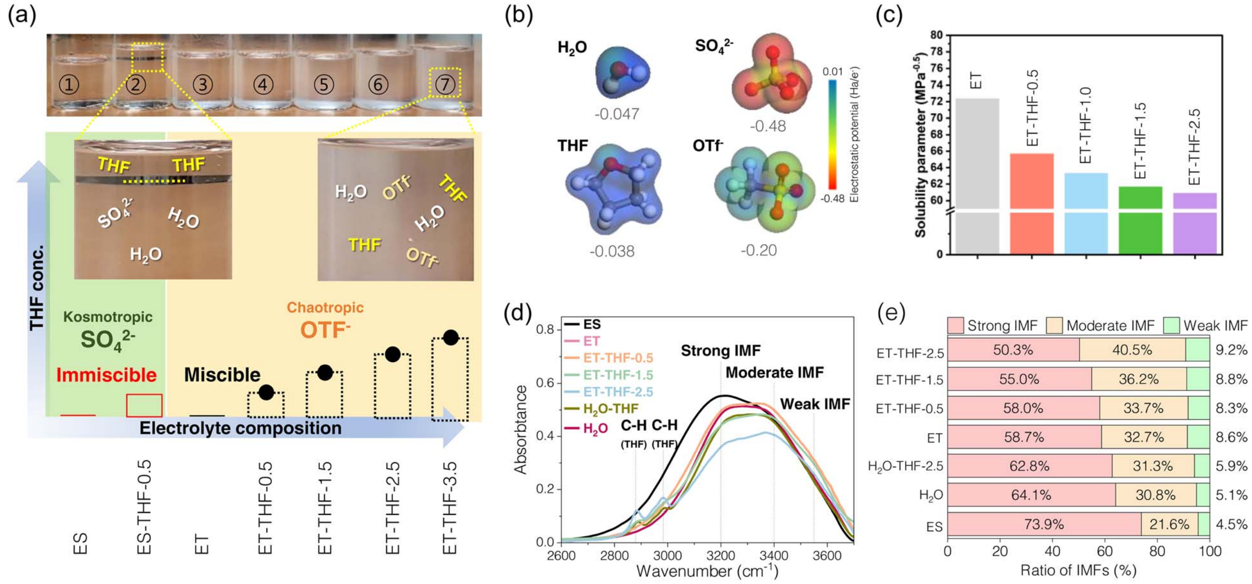

Fig. 1 Design of electrolytes for AZIBs based on intermolecular interactions between THF and anions. (a) Miscibility test of THF–H_2O solution depending on the type of zinc salt anions. (b) Estimated ESPs of the solvents and salts used in this study. (c) Hildebrand solubility parameters estimated from MD trajectory analysis of various electrolyte solutions. (d) FT-IR spectra of the different electrolyte solutions considered, and (e) analysis on the fractions of intermolecular forces in each electrolyte system.

anions enter the coordination sphere of Zn^{2+} in THF-rich solutions (Fig. 2c and d), for example, forming an average solvation environment of approximately $[Zn(H_2O)_{5.0}(THF)_{0.1}(OTf^-)_{0.9}]^{2+}$ in the case of **ET-THF-2.5.** This mixed but still water-dominated solvation environment is accompanied by a reorganization of the hydrogen-bonding network, characterized by reduced water–water connectivity and a weakened, more fragmented hydrogen-bonded structure (Fig. S3). These trends are consistent with the FT-IR and Raman spectroscopic analyses. In particular, the binding energy between Zn^{2+} and THF

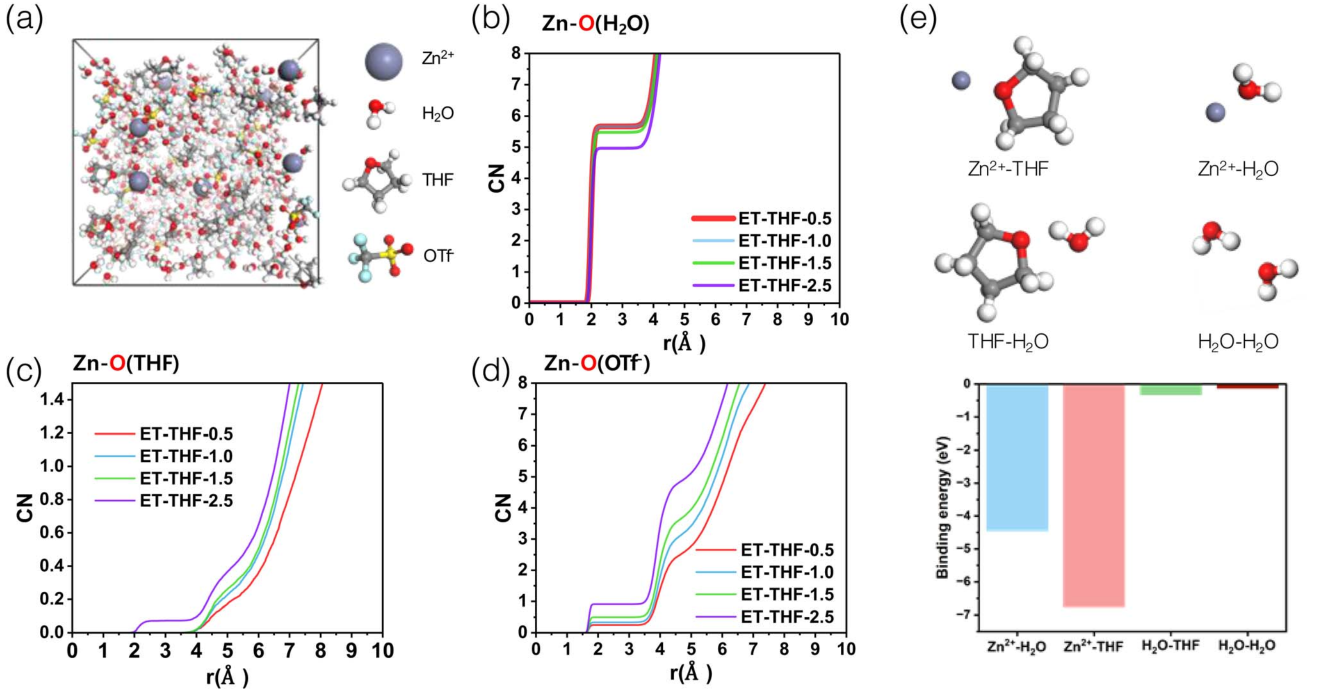

Fig. 2 Molecular dynamics (MD) simulation results for the **ET-THF** electrolyte series. (a) MD snapshot of **ET-THF-2.5**. (b) Coordination number (CN) of Zn^{2+}–H_2O, (c) CN of Zn^{2+}–THF, and (d) CN of Zn^{2+}–OTf^- in the **ET-THF** series. (e) Structure model and binding energy of Zn^{2+}–THF, Zn^{2+}–H_2O, THF–H_2O, and H_2O–H_2O.

was estimated to be much higher than that of Zn^{2+}–H_2O, as well as the interactions between solvent molecules of the same kind (Fig. 2e), thereby facilitating the incorporation of THF molecules as well as OTf^- into the Zn^{2+} solvation shell. This substitution could affect the diffusion kinetics of Zn^{2+} by the bulkier THF/OTf^- molecules compared to H_2O. Moreover, the stronger Zn^{2+}–THF binding may increase the activation energy barrier required for de-solvation during Zn plating, resulting in a higher overpotential. Consequently, the altered coordination environment is expected to influence the dynamics of key interfacial processes, such as adsorption behaviour, surface stability and charge-transfer kinetics of Zn^{2+} at the anode.

Protection of the electrode surface *via* co-solvent addition

Fig. 3a compares estimated HOMO and LUMO levels of H_2O and THF solvent. The higher LUMO level of THF indicated the higher reductive stability of THF solvent during the metal plating–stripping compared to water as mentioned earlier. Moreover, the adsorption energy of THF on major crystal facets of interest in zinc metal was evaluated (Fig. 3b), exhibiting that THF may preferentially preside on (101) and (002) facets of Zn metal deposits over water molecules, protecting the pristine surface as described in Fig. 3c and d, while on (100) facets (Fig. 3e), water and THF might compete for the adsorption. These adsorbate layers of THF may hinder active free water molecules to contact directly with the pristine Zn surface as snapshots after the relaxation step on Zn (101) surface from MD studies predicted thick THF-rich protective layers of ~3.5 nm on Zn metal (Fig. S4). Moreover, as previously noted, stronger hydrogen bonds between THF and water (Fig. 2e) may leave water molecules bound to THF to some extent, reducing the activity of water. Therefore, it is likely that the addition of THF co-solvent will lead to a reduction in the H_2O decomposition rate on Zn surface.

The actual corrosion behaviour of zinc metals in the **ET-THF** electrolyte series was monitored by assembling Zn||Cu asymmetrical cells, carrying out Zn plating–stripping for 29 cycles to achieve stable high efficiency over 99% (Fig. 4a), and plating 0.5 mAh cm^{-2}, which was subject to a resting period for 48 h before stripping (Fig. 4b). Then, spontaneous corrosion was allowed to occur at the open circuit potential (OCV) during the idle period, so that the coulombic efficiency (CE) of the final cycle would reflect the extent of zinc metal corrosion.[39,40] The efficiency was observed to be 75–85% for the **ET-THF** electrolyte series as opposed to almost 0% for pure aqueous solution (**ET**). This reflects the reduced activity of water molecules in **ET-THF**, resulting from the disruption of the hydrogen bonding network in water clusters and the protective character of THF adsorbed on zinc metal. To further confirm these beneficial effects, fresh zinc metal was put into the electrolytes containing **ET** and **ET-THF-1.5**, respectively, for a period of 2 days. For zinc metal in **ET**, the surface of zinc metal was severely corroded (Fig. 4c$_{ii}$ and S5), being covered with the white, thick, porous corrosion product of $Zn(OH)_x(OTf)_y$ (ZOT, identified from the XRD patterns).[41–44] In contrast, zinc metal in **ET-THF-1.5** retained an initial, smooth, shiny surface, indicating the surface was well-protected (Fig. 4c$_{iii}$ and S6). XPS depth profiling analysis of Zn foil soaked in each electrolyte (Fig. S7 and S8) also confirmed that **ET-THF-1.5** formed a much thinner surface SEI film, indicating a reduced Zn corrosion rate. Furthermore, the significantly reduced intensity of major crystal planes like (002), (100), and (101) peaks for the zinc metal in **ET** may indicate that the surface of zinc metal was severely corroded and covered with corrosion products. Moreover, the amount of H_2 was monitored for the electrochemical cells, where zinc metal was in contact with the electrolytes for 12 h at OCV. As the amount of THF increases, a sharp decline in H_2 gas evolution was observed (Fig. 4d). The corrosion potential and the current density based on mixed potential theory was estimated from the potentiodynamic polarization curves of zinc metal in each electrolyte (Fig. 4e). While the corrosion potential remained relatively unaltered (showing only a marginal positive shift) due to simultaneous reduction in the exchange currents for both Zn/Zn^{2+} and H_2/H^+, the corrosion current density was significantly reduced in the THF-containing electrolytes, reflecting a substantial decrease in the kinetics of H_2 evolution in the co-solvent solution. These experiments shared a common result of the effectiveness to mitigate corrosion of zinc metal of the **ET-THF** electrolyte series.

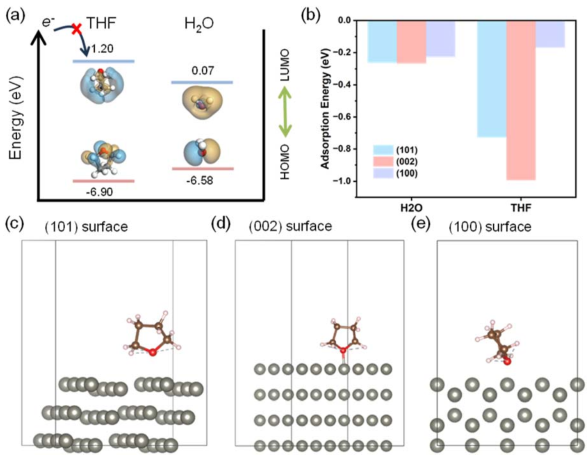

Fig. 3 Result of DFT calculations for molecule and interface reactions. (a) HOMO/LUMO levels of H_2O and THF. (b) Adsorption energy values and (c–e) schematic of THF adsorption on the three different Zn metal surfaces, (101), (002), and (100), respectively.

Zn plating–stripping behaviour in THF–H_2O electrolytes

Zn plating–stripping behaviour in single-(**ET**) or co-solvent (**ET-THF**) electrolytes was investigated with Zn||Cu asymmetrical configurations in 2 mA cm^{-2}/2 mAh cm^{-2} (Fig. 5 and S9). Generally, a bit higher overpotential (by 10–20 mV) was recorded for the **ET-THF** electrolyte series (Fig. 5a). This can be likely ascribed to the slightly reduced ionic conductivity of **ET-THF** electrolytes (Fig. S10) as well as the presence of a THF adsorbate layer on Zn deposits, which slightly impedes the surface transport of Zn^{2+}. However, while short-circuiting occurred after only 20 cycles in the cells with pure aqueous electrolyte (**ET**), stable cycling was maintained for more than 1000 h with **ET-THF** co-solvent electrolyte (Fig. 5b), during which the associated overpotential increased just slightly. This suggests that the dendritic growth of Zn deposits occurred readily during the early cycles

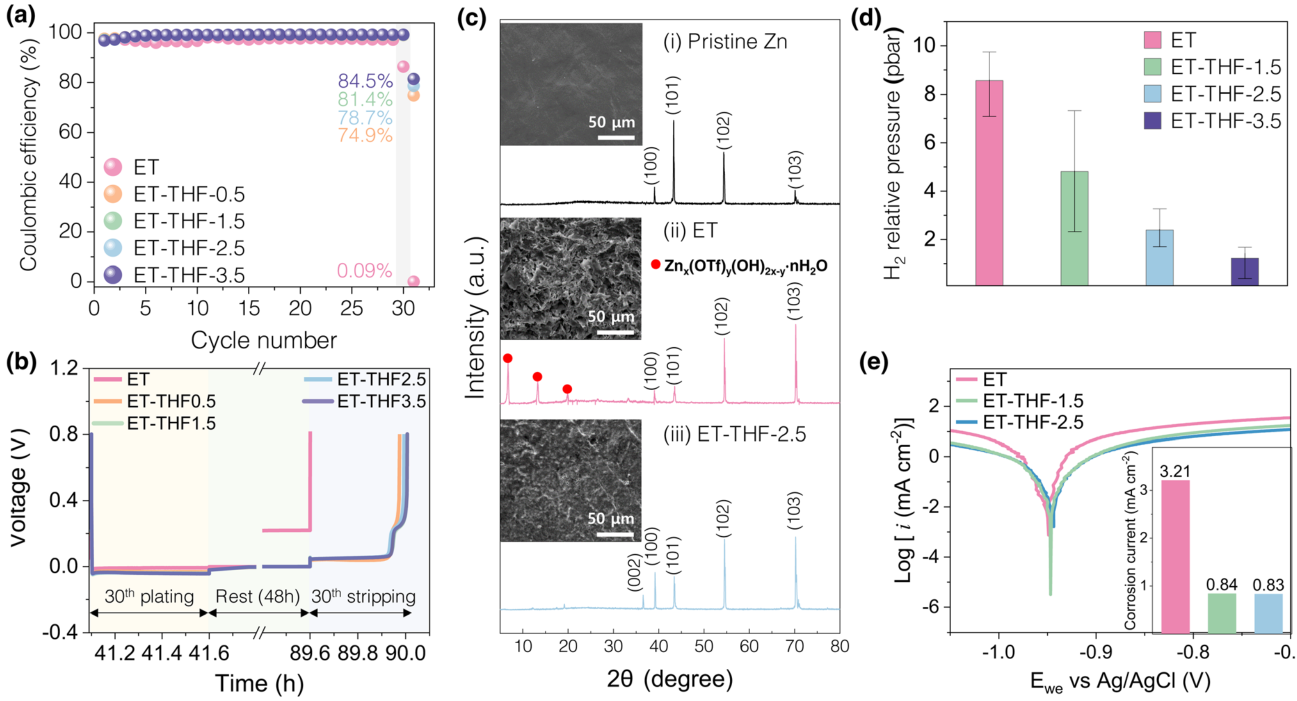

Fig. 4 Corrosion characteristics of zinc foil in the **ET-THF** electrolyte series. (a) CEs for plating–stripping for initial 29 cycles, and the 30th cycle that has a 48 h intermediate idle period between plating and stripping, and (b) the associated voltage profiles. (c) XRD patterns for (i) pristine Zn foil and those immersed in the electrolytes, (ii) **ET** and (iii) **ET-THF-2.5** for 48 h with inset figures showing the respective surface morphology. (d) Amount of H_2 evolution for Zn foil immersed in the **ET-THF** series measured by DEMS. (e) Potentiodynamic polarization curves of zinc foil in the **ET-THF** series with estimated corrosion current density.

with the **ET** electrolyte, due to spatial heterogeneity in the areal impedance caused by the uneven accumulation of corrosion products (Fig. 4c$_{ii}$, S5 and 6a). Conversely, in the **ET-THF** electrolyte series, morphological regulation was effectively controlled by the protective THF adsorbate layer; as further evidenced by the actual morphological observation in Fig. 6b and c. In **ET** electrolyte, Zn deposit (obtained after 20 cycles) looked like a highly irregular, porous heap of corrosion products. This implies that the fast corrosion rate of Zn metal and pileup of ZOT precipitates on the surface in **ET** electrolyte created uneven impedance growth on Zn metal that led to a local current spike and dendritic growth of Zn metal. On the other hand, in the **ET-THF** electrolyte series, uniform Zn platelets with well-developed crystal facets were densely packed, likely aided by the compact THF adsorbate layer that helped maintain a clean and uniform surface condition. Slightly larger crystallites were observed for the electrolyte with a higher fraction of THF in co-solvent, indicating that particle growth was kinetically favoured over nucleation in THF-rich solution. This could be attributed to the incorporation of bulky THF molecules in solvation shells, which could modify the diffusion and adsorption behaviour of Zn^{2+} on the anode. The comparison of XRD patterns for the Zn deposits after cycling in **ET** or **ET-THF** electrolyte (Fig. S11) showed that the (002) peak was particularly intense in the **ET-THF** electrolyte series. This indicates a preferential orientation, consistent with a high RTC value estimated for the (002) plane (Fig. S12), and the observation that platelets with (002) facets in **ET-THF** generally expose their (002) facets upward (Fig. 6b and c). Such behaviour can be ascribed to the strong adsorption of THF molecules on the (002) surface.

The average CE for Zn plating–stripping remained 99.47% for **ET-THF-2.5** (Fig. 5b), indicating that parasitic reactions were well suppressed in this electrolyte. Then, the cycling stability of Zn‖Zn symmetrical cells was subsequently evaluated under a stringent controlled depth of discharge (DOD) condition. For a DOD of 25% (*i.e.*, 3 mA cm^{-2}/3 mAh cm^{-2}), stable cycling was achieved up to 400 h (200 cycles), whereas at a milder DOD of 20% (*i.e.*, 2 mA cm^{-2}/2 mAh cm^{-2}), cycling could be maintained for over 600 h (300 cycles), demonstrating the high efficiency and well-controlled morphology in the **ET-THF** series. On the contrary, in **ET**, short-circuiting occurred at very early cycle, *i.e.*, at the 30th and 50th cycle, respectively, likely due to unregulated dendritic growth on the zinc surface. The performance was compared with previously reported systems in terms of DOD and cumulative capacity achieved (Fig. S13). Notably, this work exhibits a higher cumulative capacity at a moderate DOD range of 20–25%. The reaction kinetics associated with Zn plating–stripping was evaluated by calculating the exchange current density, i_o, associated with the reaction under varying electrolyte conditions. As shown in Fig. 5d, i_o decreased substantially with increasing THF fraction in the **ET-THF** series, likely due to both the reduced conductivity of the electrolyte and the higher desolvation energy cost of Zn^{2+} caused by the stronger Zn^{2+}–THF binding as more THF molecules enter the solvation shell. Accordingly, the THF content in the electrolyte should be carefully adjusted by balancing interfacial

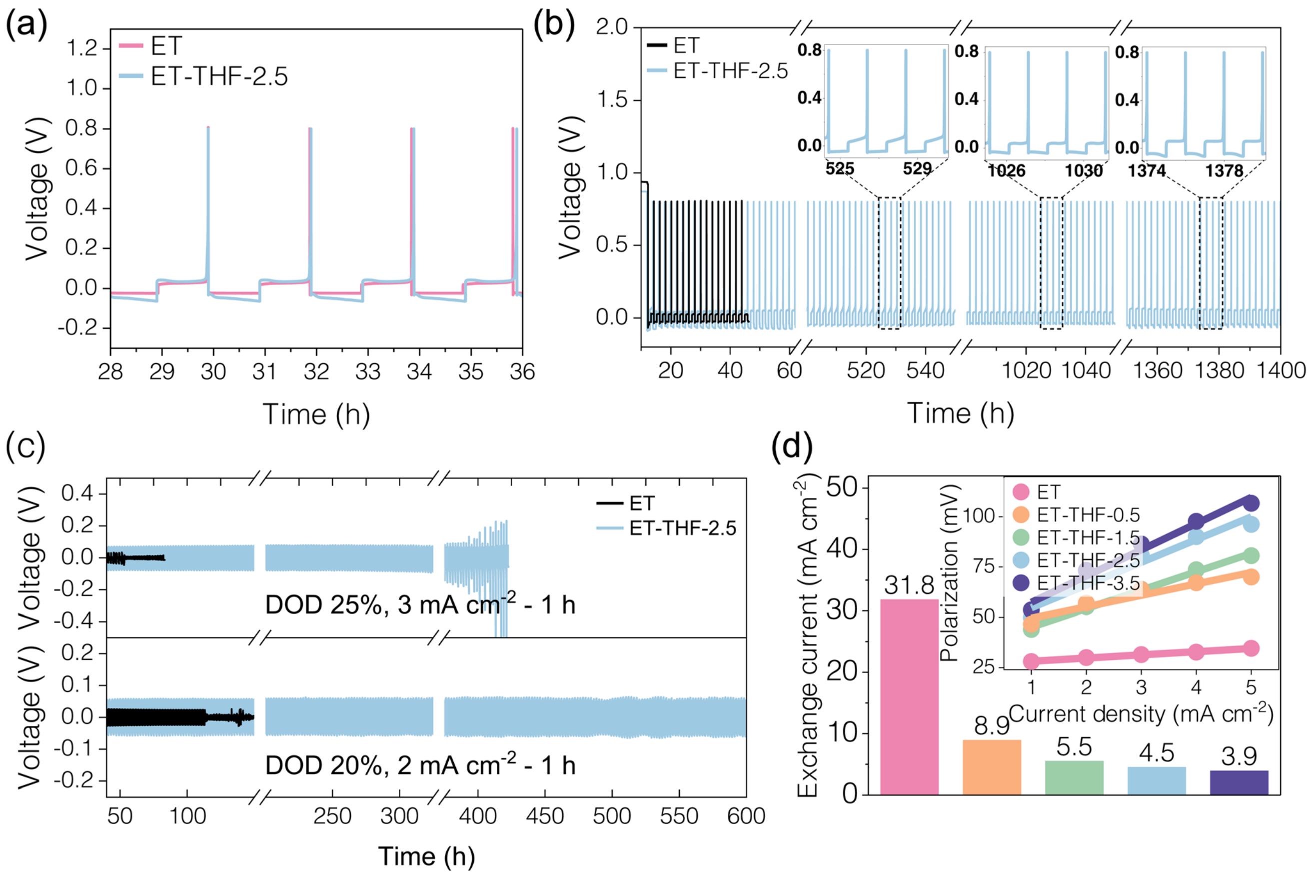

Fig. 5 Zn plating–stripping characteristics in **ET** and **ET-THF-2.5**. (a) Zn plating–stripping profiles in asymmetrical cells (Zn‖Cu) with 2 mA cm^{-2}/2 mAh cm^{-2} condition, and (b) long-term cycling behaviour in **ET** and **ET-THF-2.5** electrolytes. (c) Zn plating–stripping profiles in symmetrical cells with DOD 25% (3 mA cm^{-2}/3 mAh cm^{-2}) and 20% (2 mA cm^{-2}/2 mAh cm^{-2}). (d) Exchange current density associated with Zn plating–stripping in the **ET-THF** electrolyte series estimated from polarizations at various current rates.

stabilization and electrochemical activity, with **ET-THF-2.5** showing a favourable balance in this study. The contact angles of the electrolytes on the zinc metal foil were investigated, exhibiting the superior zincophilic character of THF-containing electrolytes (Fig. 6d). As the THF content in the electrolyte increased, the contact angles decreased sharply, which may reflect stronger adsorption of THF over water on the major crystallographic facets of zinc. This feature is expected to provide a kinetic advantage in Zn anode reactions.

Battery performance with co-solvent electrolytes

To verify the practical applicability of **ET-THF** electrolytes to AZIBs, their oxidative stability was first evaluated by linear sweep voltammetry (LSV, 25 mV s^{-1}) measurement, which revealed no significant differences with the normal simple aqueous electrolyte (Fig. S14). Then, full cells were manufactured based on the ammonium vanadate ($NH_4V_4O_{10}$, NVO) cathode and zinc metal anode. NVOs are common layer-structured insertion cathode materials for Zn^{2+} with a reversible capacity around 400 mAh g^{-1}. In this work, NVO nano-rods (Fig. S15) were synthesized *via* a hydrothermal route.[45,46] Fig. 7a shows the cycling performance of the full cells under various electrolyte conditions at 1 C current rate (1 C = 400 mA g^{-1}) between 0.2 and 1.6 V. NVO delivered an initial discharge capacity of *ca.* 400 mAh g^{-1} with a sloping potential around 0.4 and 1.2 V regardless of electrolyte type (Fig. S16). However, for **ES** or **ET** electrolyte with no THF addition, the sharp capacity fading was observed during the initial 300 cycles, which could be mostly attributed to corrosion and impedance rise of the zinc anode. In contrast, the full cell with **ET-THF** co-solvent electrolytes showed much improved capacity retention and retained original voltage profiles for more than 1000 cycles as THF efficiently protects the Zn anode surface. The reversible capacity and voltage profiles at high current rates (Fig. 7b and S16), also showed that the **ET-THF** series enabled stable cycling even at a high current rate of 10 C (=4 A g^{-1}). The slow capacity decay during the initial cycles, regardless of electrolyte type (Fig. 7b), is likely attributed to the structural reorganization of NVOs, such as Zn^{2+} trapping (Fig. S17) and interlayer expansion (Fig. S18),[47] as well as transient interfacial effects before complete stabilization by THF adsorption.

Biphasic electrolytes based on immiscibility between kosmotropic and chaotropic species

The distinct kosmotropic and chaotropic interactions among SO_4^{2-}, THF, OTf$^-$ in **ES** and the **ET-THF** series, and consequent

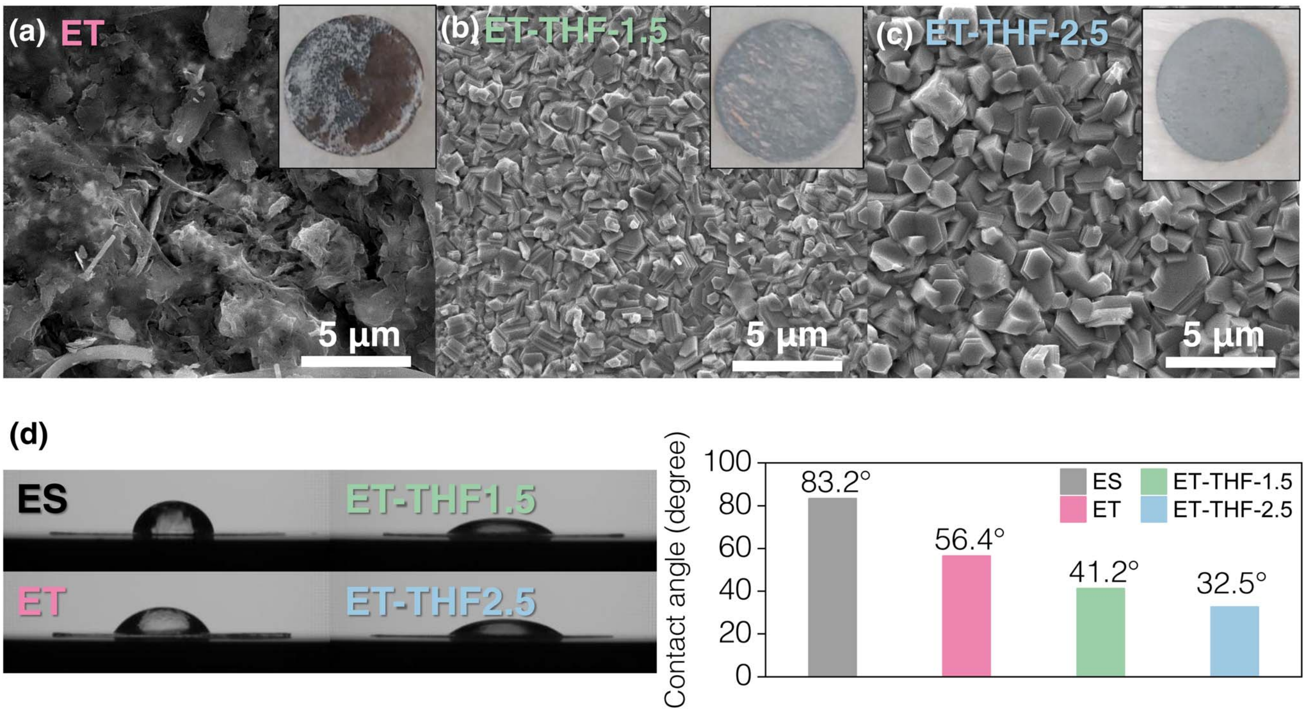

Fig. 6 Morphology of the Zn deposit and contact angles in **ET** and the **ET-THF** series. Morphology of the Zn deposit obtained after 20 cycles of plating–stripping in (a) **ET**, (b) **ET-THF-1.5**, and (c) **ET-THF-2.5**, respectively. (d) The contact angle measurement in the Zn substrate with **ES**, **ET**, and the **ET-THF** series.

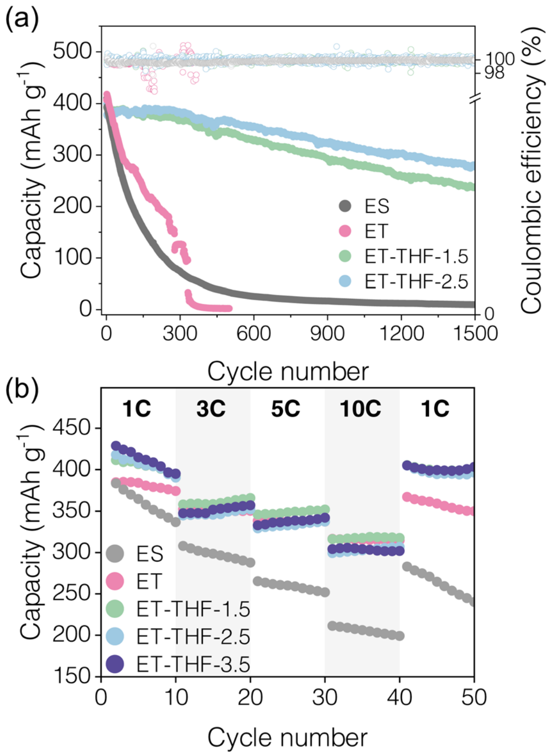

Fig. 7 Full cell characteristics with ammonium vanadate, $NH_4V_4O_{10}$, cathode in various electrolytes, **ES**, **ET** and the **ET-THF** series. (a) Cycling performance at 1 C (=400 mAh g^{-1}) up to 1500 cycles and (b) high rate performance.

mutual immiscibility of the electrolyte solutions provide an interesting opportunity of the designing biphasic electrolyte system consisting of **ES** as an anolyte and **ET-THF** as a catholyte. The design of biphasic electrolytes has recently emerged as a promising strategy to improve battery performance, as it allows tailoring electrolytes to the specific requirements of individual electrodes.[48,49] The salting-out effect of aqueous $ZnSO_4$-based solution containing THF can offers a simple route to construct a biphasic electrolyte system.[50–52] In this work, a sharp phase boundary was instantly formed even when they were blended thoroughly, where **ET-THF-2.5** with lower liquid density was spontaneously placed above **ES** as shown in Fig. 8a. Interestingly, this phase boundary showed a slight downward shift during the first 10 min after mixing, but remained stable thereafter (Fig. 8b). This was likely caused by upward mass transfer of water molecules across the phase boundary, which served as a semi-permeable membrane, allowing the selective transport of water molecules as in a reverse osmosis system,[53] under the pressure exerted by the **ET-THF** solution. The ionic conductivity of the biphasic solutions (denoted as **ES|ET-THF**) was measured to evaluate ion transport across the phase boundary, yielding 27.4 mS cm^{-1} (compared to 50.5 for **ES** and 31.7 for **ET-THF-2.5**, Fig. S10). The moderate decrease, likely due to the water-dominated Zn^{2+} solvation structure across the phase boundary, does not significantly compromise its function as an electrolyte for AZIBs. The actual applicability of this biphasic electrolyte to zinc-ion batteries was evaluated by using a $Zn–I_2$ system – as a proof-of-concept study – in which the electrolyte must meet distinct and often conflicting

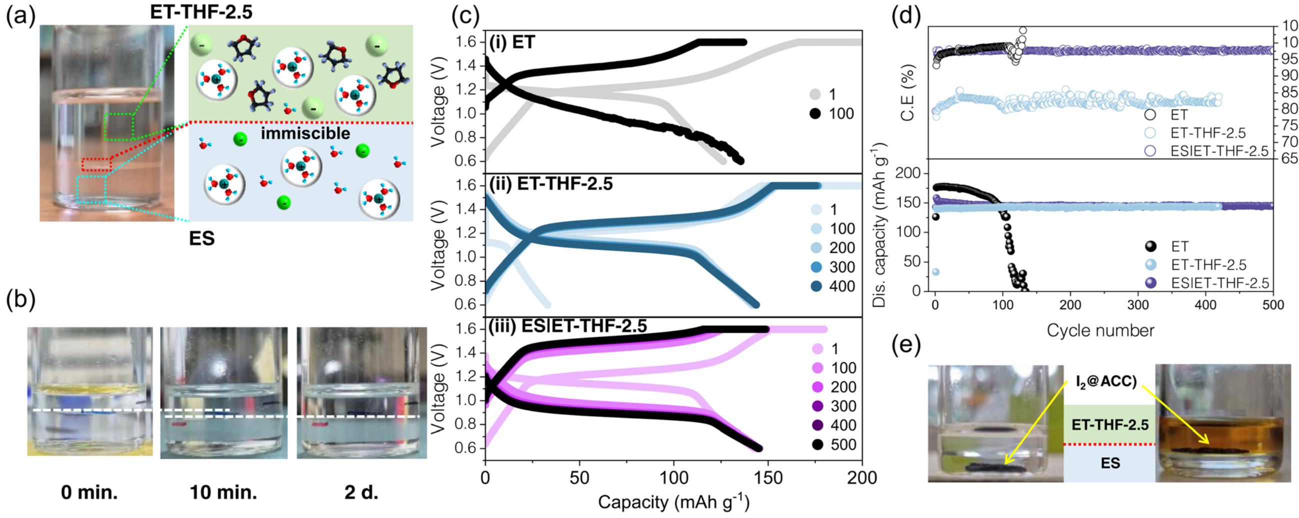

Fig. 8 Preparation of a biphasic electrolyte *via* the THF salting-out effect from a sulfate solution and its application in a Zn/I_2 battery. (a) Photograph of a biphasic electrolyte composed of **ES** (lower layer) and **ET-THF-2.5** (upper layer) electrolytes. (b) Stability of the phase boundary over time. (c) Discharge–charge profiles of Zn–I_2 cells employing (i) **ET**, (ii) **ET-THF-2.5**, and (iii) **ES**|**ET-THF-2.5** biphasic electrolytes, and (d) the corresponding cycling performance up to 500 cycles. (e) Iodine solubility from the I_2@ACC cathode depending on the location within the biphasic electrolyte.

requirements for each electrode. Herein, **ET-THF** was utilized as an anolyte to regulate the anode reactions as described in previous sections, while **ES** was served as a catholyte to suppress I_2 dissolution and polyiodide (I_3^-, I_5^-) shuttle effectively, which was one of main technical challenges on the cathodes in a Zn–I_2 battery.[54,55] Herein, I_2@active carbon cloth (ACC) composite cathodes were manufactured with an areal capacity of ~2.3 mAh cm^{-2} *via* melt-impregnation in a closed plastic container. Fig. 8c and d show the voltage profiles and cycling performance of Zn–I_2 cells with **ET**, **ET-THF-2.5**, and **ES**|**ET-THF**, respectively. With **ET** electrolyte, the cells delivered a large capacity of ~180 mAh g^{-1} with a relatively good CE (97.91%), but faded rapidly during the incipient cycles, since the Zn anode was prone to corrosion with this electrolyte. In contrast, the cells with **ET-THF-2.5** were featured with a slightly reduced reversible capacity of ~150 mAh g^{-1}, and a much lower CE of ~80%. The lowered capacity and CE were primarily caused by the higher solubility of I_2 from the cathode in **ET-THF** solution (Fig. 8d), which could trigger a polyiodide shuttling and a self-discharge. It is likely that much more stable cycling performance was ascribed to the well-protected anode by THF adsorbates, despite those serious issues at the cathode. Fig. 8c$_{\text{iii}}$ shows the electrochemical performance of the cell with the **ES**|**ET-THF** biphasic electrolyte. Remarkably, the cell exhibited a distinct synergistic effect, accomplishing both high efficiency and long-term cyclic stability of the I_2 cathode. As shown in Fig. 8e, the I_2/ACC cathode immersed in the **ES** region in the **ES**|**ET-THF** biphasic electrolyte retained a transparent solution, while the cathode in **ET-THF** showed unique coloring by the dissolved I_2 species.[56] Therefore, the excellent performance was likely attributed to the tailored solution at each electrode in the biphasic electrolyte. The increased voltage hysteresis observed with a biphasic electrolyte can be attributed to additional polarization arising from ion transport across the phase-boundary and from liquid junction potentials involving iodine species.

Conclusions

In this study, we have demonstrated that the rational design of the electrolyte systems based on intermolecular interactions among electrolyte components can offer a promising strategy to address various challenges in AZIBs. By considering the kosmotropic and chaotropic properties of co-solvent (THF) and anions (triflate and sulfate), we designed a fully miscible electrolyte system that reduces water activity and forms protective adsorbate layers on the metal surface that effectively mitigate various interfacial instabilities. Moreover, intentional immiscibility can be utilized to constitute biphasic customized to each individual electrode in AZIBS, offering new insights and opportunities to tackle longstanding challenges with various AZIBs.

Material and methods

Material preparation

Synthesis of ZOT. The zinc hydroxide triflate compound ($(Zn(OH)_x(OTf)_y$, ZOT) was prepared by a precipitation method. 10 mL of 0.5 M NaOH aqueous solution was slowly added into 10 mL of 1.0 M $Zn(OTF)_2$ aqueous solution with stirring at 300 rpm at room temperature. The precipitate powder was filtered, followed by drying in an oven for 24 h at 80 °C.

Synthesis of NVO. Ammonium vanadate ($NH_4V_4O_{10}$) was synthesized by a hydrothermal method. 1.170 g of ammonium metavanadate (NH_4VO_3) was dissolved in 50 mL of deionized water at 80 °C. Then, maintaining the solution temperature at 80 °C, 1.891 g of oxalic acid dihydrate ($H_2C_2O_4 \cdot 2H_2O$) was slowly added to solution with magnetic stirring at 200 rpm for 30 min. The resulting solution was moved into a 50 mL Teflon-lined stainless-steel autoclave and heated at 140 °C for 48 h. After cooling to room temperature, the products were collected by centrifugation (5000 rpm, 7 min.) and washed several times with deionized water. Finally, the obtained solids were dried at 80 °C overnight to collect the $NH_4V_4O_{10}$ powder.

Electrochemical measurements

To prepare the $NH_4V_4O_{10}$ cathode electrode, an $NH_4V_4O_{10}$ slurry was mixed with 70 wt% of the active material ($NH_4V_4O_{10}$), 20 wt% Super P carbon as a conductive agent, and 10 wt% polyvinylidene fluoride (PVdF) as a binder in N-methyl-2-pyrrolidone (NMP). To homogenize these materials, a ball-milling system (Mini-Mill Pulverisette 23, Fritsch) was used for 40 min at 40 Hz. Then, the homogenized slurry was coated onto titanium foil (99.7% metals basis) with a 150 μm doctor blade, targeting an active material loading of approximately 1.2 mg cm^{-2}. Subsequently, the electrode was dried in a convection oven at 80 °C for 24 h.

To prepare the I_2@ACC electrode, iodine powder was dispersed uniformly in ACC, which was transferred to a closed plastic container, being subject to a heat treatment at 90 °C for 6 h. The typical loading of I_2 on ACC was 9–11 mg cm^{-2}.

To evaluate the electrochemical performance of Zn‖$NH_4V_4O_{10}$ full cells, CR2032 coin cells were assembled. Each cell consisted of a $NH_4V_4O_{10}$ cathode (12 mm in diameter), a zinc foil anode (14 mm in diameter, 0.1 mm thickness), a glass microfiber filter (GF/C, Whatman) as the separator, and each electrolyte. Galvanostatic charge–discharge (GCD) tests were performed between 0.4–1.6 V at a rate of 1 C (1 C = 400 mA g^{-1} based on $NH_4V_4O_{10}$) with a MACCOR battery cycler. For Zn‖I_2@ACC full cells, charge–discharge was performed similarly between 0.6 and1.6 V at a rate of 1 C (1 C = 211 mA g^{-1} based on I_2).

For Cu‖Zn asymmetric cells, CR2032 coin cells were prepared with copper foil (0.02 mm thickness) as the working electrode and zinc foil (0.1 mm thickness) as the counter electrode with the given electrolytes. GCD was carried out at current densities of 1, 2, and 3 mA cm^{-2} with a cutoff voltage of 0.8 V.

Zn‖Zn symmetric cells were fabricated in CR2032 coin cells. Pieces of zinc foil (0.05 mm thickness, Hosen) were used as both electrodes with each electrolyte. For depth-of-discharge (DOD) testing, a Zn‖Cu half-cell was first assembled using Cu foil (0.02 mm thickness) and then zinc was electrodeposited onto the copper with a capacity equal to half of a Zn foil electrode. The Zn plated Cu electrode is used with Zn foil to complete the symmetric cell. GCD was conducted at current densities set for specific DOD values within −0.8 to 0.8 V.

To evaluate the time-dependent corrosion behavior of zinc in different electrolytes, the test was investigated by using Cu‖Zn asymmetric cells. Zinc foil (0.05 mm thickness, 14 mm diameter) was used as the reference/counter electrode and copper foil (0.02 mm thickness, 14 mm diameter) as the working electrode. The plating/stripping process of Zn on Cu foil was performed between −0.2 and 0.8 V at 1 mA cm^{-2} for 30 min (0.5 mAh cm^{-2}) using a MACCOR cycler. After 30 cycles, a 31st plating of Zn on Cu foil was conducted followed by resting for 48 h to monitor the open-circuit potential (OCP). A final stripping step was then carried out to evaluate the extent of Zn corrosion.

Exchange current density was calculated from a simplified Tafel-equation. The average overpotential value was extracted from the Zn symmetrical cell by repeating 5 cycles at each current density of 1, 2, 3, 4, and 5 mA cm^{-2}.

Cyclic voltammetry (CV) was carried out with a potentiostat/galvanostat (BioLogic VMP3). The scan was carried out from 0.25 V (*vs.* OCP) to −1.2 V (*vs.* Ag/AgCl) at 0.05 mV s^{-1}. Corrosion potential (E_{corr}) and corrosion current density (I_{corr}) were obtained from the extrapolation of Tafel slopes within ±100 mV of E_{corr}.

Ionic conductivity was measured *via* electrochemical impedance spectroscopy (EIS) at 25 °C using two stainless steel blocking electrodes in each electrolyte. The measurements were conducted using a BIOLOGIC VMP3 over a frequency range of 10^5 to 10^{-2} Hz with an amplitude of 10 mV. A relative comparison method was applied to calculate the ionic conductivity of each electrolyte based on the known value of 2.0 M $ZnSO_4$.

Characterization

The surface morphologies were observed by field emission scanning electron microscopy (FE-SEM, Inspect F50, FEI Corp). The crystal structure of samples was investigated by X-ray diffraction (XRD, Rigaku d/MAX-2500/PC) using Cu-Kα radiation (λCu-Kα = 1.5405 Å) by step scanning (2° min^{-1}) in the 2θ range of 5–80°. To evaluate the intermolecular force of each electrolyte, Fourier transform infrared absorption (FT-IR) analysis was carried out (ThermoFisher Nicolet iS10 ATR(Ge), DTGS detector).

XPS measurements were performed using a Nexsa spectrometer (Thermo Fisher Scientific) equipped with a monochromated Al Kα source (1486.6 eV, 72 W, 12 kV) at a base pressure of 2.0×10^{-8} mbar. The binding energies were calibrated against the C 1s peak at 284.8 eV. For depth profiling, Ar^+ sputtering was performed at 2 kV with a rate of ∼0.5 nm s^{-1}, and surface spectra were acquired after sputtering for 20 s.

The contact angle of electrolytes on the zinc metal surface was measured using a contact angle goniometer (Osilia Co.). 5 μL of electrolyte was dropped onto the zinc surface, and the contact angle was measured after a 5 second stabilization period.

To investigate hydrogen evolution under open-circuit conditions, *in situ* quantitative gas monitoring was carried out using a DEMS system (HPR-20 R&D, Hiden Analytical). For this purpose, modified coin-type cells were fabricated, in which the bottom case contained a 0.5 mm central aperture and a mesh-type current collector, enabling gas transfer. The cell was assembled with a stainless-steel (or nickel) mesh, a glass fiber separator (GF/C), and a Zn foil electrode, followed by the injection of 200 μL electrolyte. The evolved gases were continuously delivered to the mass spectrometer at a constant flow of 15 mL min^{-1}, and the accumulated species were analyzed every 4 h during resting periods.

Computational details

Molecular dynamics (MD) simulation. The MD simulations for high-concentration electrolytes with the diluent were performed using BIOVIA Material Studio 2021 of Accelrys Inc.[57] All calculations were performed using the COMPASSIII force field, the latest for simulating liquid species.[58] The amorphous structure of aqueous liquid electrolyte was set iteratively to construct the stable system using the Amorphous cell calculation module. The simulation cell used in this simulation contains salt of 1 M $Zn(OTf)_2$ and solvent molecules of H_2O according to the cosolvent concentration of THF. The cells of **ET**, **ET-THF-0.5**, **ET-THF-1.0**, **ET-THF-1.5**, and **ET-THF-2.5** have 8, 8, 9, 10, 13 $Zn(OTf)_2$, 300 H_2O and 0, 15, 30, 45, 75 THF cosolvent molecules, respectively, applying periodic boundary conditions. Cell relaxation and production runs were conducted using an NPT (isothermal–isobaric) ensemble at a pressure of 1 bar, and room temperature through the implementation of the Berendsen barostat and Nose–Hoover thermostat. The pre-relaxation step sequence is performed for 50 ps and then relaxation for 2 ns. For analyzing the H_2O population and around solvation structure, the radial distribution function (RDF) is calculated for the relaxation step divided by 1 fs. The coordination number (CN), denoted as $n(r)$, for molecules was calculated using RDF, denoted as $g(r)$. The RDF and CN are given by:

$$g(r) = \frac{\mathrm{d}n(r)}{4\pi \mathrm{d}r\rho(r)}$$

$$n(r) = \int_0^r 4\pi r^2 g(r)\rho(r)\mathrm{d}r$$

where the distance between atoms and the local density of atoms is denoted by r and $\rho(r)$, respectively.[59] The following equation was used to calculate the Hildebrand solubility parameters denoted by δ:

$$\delta = \sqrt{E_{\mathrm{CED}}}$$

$$E_{\mathrm{CED}} = \frac{\Delta H_{\mathrm{v}} - RT}{V}$$

where E_{CED}, ΔH_{v}, V, and T are cohesive energy density, heat of vaporization, volume, and absolute temperature.[60]

Density functional theory (DFT) calculation. The DFT calculations are performed using the Dmol3 package and Vienna *Ab Initio* Simulation Package (VASP). The electrostatic potential (ESP) value, binding energy, and HOMO/LUMO calculation are analyzed with the B3LYP functional using the double numerical plus polarization (DNP) numerical basis set.[61–63] The maximum energy and force convergence tolerance were set by 1.0×10^{-5} and 0.002 Ha Å^{-1}, respectively. The self-consistent field tolerance was set below 1.0×10^{-6} for atomic potential. The following equation was used to calculate the binding energy:

$$E_{\text{binding energy}} = E_{\mathrm{T}} - \sum_{i=1}^{N} E_i$$

where N, E_{i}, and E_{T} represent a number of components that form the total structure, the energy of each molecule, and the total energy of the diluent structure, respectively.

The adsorption energy and interface reaction were calculated using VASP.[64] These calculations were based on the Perdew–Burke–Ernzerhof (PBE) functional within the framework of generalized-gradient approximation (GGA) and employed Projector-Augmented Wave (PAW) pseudopotentials. The k-point mesh for sampling the Brillouin zone in the Monkhorst–Pack scheme was set at 3 × 3 × 3, and the energy cutoff was set at 520 eV. Optimizing the geometry and energy convergence was based on achieving complete atomic relaxation and meeting the breaking condition for electronic self-consistency loop requirements until the forces and energy for every atom were below 10^{-2} eV Å^{-1} and 10^{-4} eV.

$$E_{\text{adsorption energy}} = E_{\mathrm{T}} - E_{\text{Zn surface}} - E_{\text{molecule}}$$

$$\Delta\rho = \rho_{\text{total}} - \rho_{\text{Zn surface}} - \rho_{\text{molecule}}$$

The adsorption energy and charge density differences were calculated using two equations where $E_{\text{Zn surface}}$ is the energy of the Zn surface for (101), (001), and (100), E_{molecule} is the H_2O and THF molecule adsorbed on the surface, and E_{T} is the total structure, respectively. In the charge density differences equation, ρ_{total}, $\rho_{\text{Zn surface}}$, andρ_{molecule} were total, absorbate, and substrate charge densities, respectively. The calculated charge density differences were visualized using VESTA software, with the iso-surface set to 0.005.

Author contributions

S. H. Oh conceived the idea, designed the experiments, and supervised the project. J. Lim performed material synthesis, characterization and battery testing. H. Chang, I. Y. Jeong and J. Moon carried out MD simulations and DFT calculations. M. Jeong, Y. Yoo, H. Baeg helped with material synthesis. T. Yim, D. Byun, K. Y. Chung, H. S. Kim contributed to the battery test and its analysis. All authors contributed to the data analysis and discussion. S. H. Oh, and J. Moon wrote the manuscript.

Conflicts of interest

There are no conflicts to declare.

Data availability

The data supporting this article have been included as part of the supplementary information (SI). Supplementary information: a nomenclature table for the electrolytes, FTIR deconvolution data, computational simulation results, and additional materials characterization data, including XPS, XRD, and RTC analyses; electrochemical data such as electrolyte ionic conductivity and supplementary cell charge–discharge performance results. See DOI: https://doi.org/10.1039/d5ta08096g.

Acknowledgements

This work was financially supported by the National Research Foundation of Korea (RS-2024-00407015 and RS-2025-25441257), KIST institutional program (2E33942), and the Open R&D program of Korea Electric Power Corporation (No. R23XH03).

Notes and references

1 M. Li, Q. Ma, R. Shan, A. Abdulla, E. Virguez, S. Gao and D. Patino-Echeverri, *Commun. Earth Environ.*, 2024, **5**, 661.
2 M. Staadecker, J. Szinai, P. A. Sanchez-Perez, S. Kurtz and P. Hidalgo-Gonzalez, *Nat. Commun.*, 2024, **15**, 9501.
3 J. T. Frith, M. J. Lacey and U. Ulissi, *Nat. Commun.*, 2023, **14**, 420.
4 F. Degen, M. Winter, D. Bendig and J. Tübke, *Nat. Energy*, 2023, **8**, 1284–1295.
5 A. Kim, Y. Park, J. Choi, S.-H. Yu and K. W. Nam, *ACS Appl. Energy Mater.*, 2025, **8**, 6806–6828.
6 G. Li, L. Sun, S. Zhang, C. Zhang, H. Jin, K. Davey, G. Liang, S. Liu, J. Mao and Z. Guo, *Adv. Funct. Mater.*, 2023, **34**, 2301291.
7 W. Du, E. H. Ang, Y. Yang, Y. Zhang, M. Ye and C. C. Li, *Energy Environ. Sci.*, 2020, **13**, 3330–3360.
8 Y. Lv, Y. Xiao, L. Ma, C. Zhi and S. Chen, *Adv. Mater.*, 2022, **34**, e2106409.
9 M. Tang, Q. Liu, X. Zou, B. Zhang and L. An, *Adv. Mater.*, 2025, e2501361, DOI: 10.1002/adma.202501361.
10 C. Xv, T. Jiang, C. Zhu, W. Gou, K. Zang, J. Jia, R. Zhang, X. Wang, G. Li and Q. Fan, *ACS Appl. Mater. Interfaces*, 2025, **17**, 41379–41402.
11 K. Zhu, W. Xie and W. Yang, *Angew Chem. Int. Ed. Engl.*, 2025, e202516233, DOI: 10.1002/anie.202516233.
12 X. Liu, Y. Zhang, L. Wang, R. Diao, T. Li, H. Sun, H. Hu, W. Xing and Z. Yan, *ACS Nano*, 2024, e30054.
13 K. Bao, M. Wang, Y. Zheng, P. Wang, L. Yang, Y. Jin, H. Wu and B. Sun, *Nano Energy*, 2024, **120**, 109089.
14 Q. Nian, X. Zhang, Y. Feng, S. Liu, T. Sun, S. Zheng, X. Ren, Z. Tao, D. Zhang and J. Chen, *ACS Energy Lett.*, 2021, **6**, 2174–2180.
15 Y. Liang, M. Qiu, P. Sun and W. Mai, *Adv. Funct. Mater.*, 2023, **33**, 2304878.
16 T. Liu, C. Lei, H. Wang, J. Li, P. Jiang, X. He and X. Liang, *Adv. Mater.*, 2024, **36**, e2405473.
17 X. Li, J. Miao, F. Hu, K. Yan, L. Song, H. Fan, L. Ma and W. Wang, *J. Mater. Chem. A*, 2024, **12**, 968–978.
18 X.-Z. Shi, Y. Zhang, R. Zhang, Y. Yu, S.-L. Tian, L. Lin and W.-Q. Liu, *Electrochim. Acta*, 2025, **540**, 147272.
19 H. Tu, X. Li, Y. Zhou, Z. Wang, R. Wu, H. Zhou, C. Meng, Y. Xue, I. Khan and A. Yuan, *ACS Appl. Energy Mater.*, 2024, **7**, 4385–4393.
20 H. Huang, J. Xu, Y. Huang, Z. He, H. Feng, C. Hu, Z. Chen, Z. Yang, T. Tian and W. Zhang, *Adv. Energy Mater.*, 2024, **14**, 2401643.
21 T. Wei, H. Zhang, Y. Ren, L. e. Mo, Y. He, P. Tan, Y. Huang, Z. Li, D. Zhu and L. Hu, *Adv. Funct. Mater.*, 2023, **34**, 2312506.
22 K. D. Collins, G. W. Neilson and J. E. Enderby, *Biophys. Chem.*, 2007, **128**, 95–104.
23 W.-Y. Kim, H.-I. Kim, K. M. Lee, E. Shin, X. Liu, H. Moon, H. Adenusi, S. Passerini, S. K. Kwak and S.-Y. Lee, *Energy Environ. Sci.*, 2022, **15**, 5217–5228.
24 S. Chen and C. Zhi, *Commun. Chem.*, 2025, **8**, 20.
25 W. He, Y. Ren, B. S. Lamsal, J. Pokharel, K. Zhang, P. Kharel, J. J. Wu, X. Xian, Y. Cao and Y. Zhou, *ACS Appl. Mater. Interfaces*, 2023, **15**, 6647–6656.
26 S. You, Q. Deng, Z. Wang, Y. Chu, Y. Xu, J. Lu and C. Yang, *Adv. Mater.*, 2024, **36**, e2402245.
27 J. Qiang, W. Yu, Y. Zhao, L. Zhang, Y. Chen, Z. Gao, Y. An, S. Le, Y. Mao and G. Zhao, *Electrochim. Acta*, 2024, **481**, 143929.
28 Y. Lin, Z. Yang, X. Zhang, Y. Liu, G. Hu, S. Chen and Y. Zhang, *Energy Storage Mater.*, 2023, **58**, 184–194.
29 M. Wang, L. Yin, M. Zheng, X. Liu, C. Yang, W. Hu, J. Xie, R. Sun, J. Han, Y. You and J. Lu, *Nat. Commun.*, 2024, **15**, 8866.
30 D. Aurbach, A. S. Z. Lu, H. G. Y. Gofer, Y. C. R. Turgeman, M. Moshkovich and E. Levi, *Nature*, 2000, **407**, 724–727.
31 D. Degoulange, R. Pandya, M. Deschamps, D. A. Skiba, B. M. Gallant, S. Gigan, H. B. de Aguiar and A. Grimaud, *Proc. Natl. Acad. Sci. U. S. A.*, 2023, **120**, e2220662120.
32 N. Dubouis, C. Park, M. Deschamps, S. Abdelghani-Idrissi, M. Kanduc, A. Colin, M. Salanne, J. Dzubiella, A. Grimaud and B. Rotenberg, *ACS Cent. Sci.*, 2019, **5**, 640–643.
33 N. J. Bridges, K. E. Gutowski and R. D. Rogers, *Green Chem.*, 2007, **9**, 177–183.
34 G. W. Castellan, *Physical Chemistry*, Benjamin/Cummings Publishing Company, Menlo Park, CA, USA, 3 edn, 1983.
35 C. M. Hansen, *Hansen Solubility Parameters: A User's Handbook*, CRC Press, 2007.
36 P. Laurson, P. Raudsepp, H. Kaldmäe, A. Kikas and U. Mäeorg, *AIP Adv.*, 2020, **10**, 85214.
37 D. Yuan, X. Li, H. Yao, Y. Li, X. Zhu, J. Zhao, H. Zhang, Y. Zhang, E. T. J. Jie, Y. Cai and M. Srinivasan, *Adv. Sci.*, 2023, **10**, e2206469.
38 L. Flores, J. F. Martin, P. Toudret, P. A. Bayle and S. Martinet, *Electrochim. Acta*, 2025, **536**, e202501601.
39 Y. Yuan, Z. Li, R. Deng, S. D. Pu, M. Walker, M. Cai, F. Wu, P. G. Bruce and A. W. Robertson, *Energy Environ. Sci.*, 2025, **18**, 5610–5621.
40 S. D. Pu, B. Hu, Z. Li, Y. Yuan, C. Gong, Z. Ning, C. Chau, S. Yang, S. Zhang, L. Pi, Y. T. Tang, J. Yue, T. J. Marrow, X. Gao, P. G. Bruce and A. W. Robertson, *Joule*, 2023, **7**, 366–379.
41 R. Chen, C. Zhang, J. Li, Z. Du, F. Guo, W. Zhang, Y. Dai, W. Zong, X. Gao, J. Zhu, Y. Zhao, X. Wang and G. He, *Energy Environ. Sci.*, 2023, **16**, 2540–2549.
42 Y. Dong, L. Miao, G. Ma, S. Di, Y. Wang, L. Wang, J. Xu and N. Zhang, *Chem. Sci.*, 2021, **12**, 5843–5852.
43 W. Wang, S. Chen, X. Liao, R. Huang, F. Wang, J. Chen, Y. Wang, F. Wang and H. Wang, *Nat. Commun.*, 2023, **14**, 5443.
44 X. Wang, L. Liu, Z. Hu, C. Han, X. Xu, S. Dou and W. Li, *Chem. Sci.*, 2024, **15**, 17348–17361.

45 Q. Li, X. Rui, D. Chen, Y. Feng, N. Xiao, L. Gan, Q. Zhang, Y. Yu and S. Huang, *Nano-Micro Lett.*, 2020, **12**, 67.

46 B. Tang, J. Zhou, G. Fang, F. Liu, C. Zhu, C. Wang, A. Pan and S. Liang, *J. Mater. Chem. A*, 2019, **7**, 940–945.

47 Z. Xing, G. Xu, J. Han, G. Chen, B. Lu, S. Liang and J. Zhou, *Trends Chem.*, 2023, **5**, 380–392.

48 X. Zhang, T. P. Pollard, S. Tan, N. Zhang, J. Xu, Y. Liu, A. L. Phan, W. Zhang, F. Chen, C. Yang, E. Hu, X. Q. Yang, O. Borodin and C. Wang, *Nat. Nanotechnol.*, 2025, **20**, 798–806.

49 Z. Wang, H. Ji, J. Zhou, Y. Zheng, J. Liu, T. Qian and C. Yan, *Nat. Commun.*, 2023, **14**, 2267.

50 J. Zou, G. Wang, S. Lin, H. Yang, X. Ma, H. Ji, S. Zhu, Y. Lyu, C. Wang, Y. Zhou, Q. He, Q. Wang, F. Gao, Z. Zhang, T. Hao, Z. Wang, Y. Zhang, X. Liu and Y. Wu, *Adv. Funct. Mater.*, 2024, **34**, 2415607.

51 H. Fan, H. Zhang, Q. Liu, M. Li, L. Liu, J. Gao, Q. Zhang and E. Wang, *ACS Energy Lett.*, 2023, **8**, 4338–4348.

52 J. Zhou, B. Hao, H. Yang, H. Ao, T. Qian, Z. Wang and C. Yan, *Nano Lett.*, 2025, **25**, 4809–4817.

53 J. Glater, *Desalination*, 1998, **117**, 297–309.

54 H. Wen, H. Wen, Y. Sun, J. Li, C. Zhuang, M. Liu, H. Li, H. Fan, B. Yin, S. Zhang and T. Ma, *Adv. Funct. Mater.*, 2025, **35**, 2500323.

55 H. Chen, X. Li, K. Fang, H. Wang, J. Ning and Y. Hu, *Adv. Energy Mater.*, 2023, **13**, 2302187.

56 H. Xu, R. Zhang, D. Luo, K. Huang, J. Wang, G. Sun, H. Dou and X. Zhang, *Energy Environ. Sci.*, 2025, **18**, 7447–7459.

57 R. L. C. Akkermans, N. A. Spenley and S. H. Robertson, *Mol. Simul.*, 2013, **39**, 1153–1164.

58 R. L. C. Akkermans, N. A. Spenley and S. H. Robertson, *Mol. Simul.*, 2020, **47**, 540–551.

59 C. Park, M. Kanduč, R. Chudoba, A. Ronneburg, S. Risse, M. Ballauff and J. Dzubiella, *J. Power Sources*, 2018, **373**, 70–78.

60 J. H. Hildebrand, *Proc. Natl. Acad. Sci. U. S. A.*, 1979, **76**, 6040–6041.

61 A. D. Becke, *J. Chem. Phys.*, 1993, **98**, 5648–5652.

62 B. Delley, *J. Chem. Phys.*, 1990, **92**, 508–517.

63 B. Delley, *J. Chem. Phys.*, 2000, **113**, 7756–7764.

64 G. F. Kresse, *Comput. Mater. Sci.*, 1996, **6**, 15–50.